

## Earthquake size distributions are slightly different in compression vs extension

Matteo Taroni <sup>1</sup>✉ & Michele Matteo Cosimo Carafa <sup>2</sup>

The earthquake size distribution is described by an exponential function governed by the b-value parameter. It has already been proven that the b-value depends on the differential stress and tectonic settings. Here, we propose a new method to group earthquakes using the kinematics of the interseismic geodetic strain rates and horizontal stress directions. We select the Italian peninsula as a case study, and we find that the b-value is significantly larger in the extensional setting than in the compressional one, although these differences are much smaller than previously reported. We also show that spatial fragmentation of uniform tectonic regimes leads to inaccurate b-value estimation due to the undersampling of earthquake size distribution. Given these results, we conclude that stress directions and geodetic data complement other geological or geophysical information and reduce the arbitrariness in drawing zones for a seismotectonic model.

<sup>1</sup>Istituto Nazionale di Geofisica e Vulcanologia, Rome, Italy. <sup>2</sup>Istituto Nazionale di Geofisica e Vulcanologia, L'Aquila, Italy. ✉email: [matteo.taroni@ingv.it](mailto:matteo.taroni@ingv.it)

The Gutenberg-Richter law<sup>1</sup> is an empirical relation that describes the distribution of the magnitudes of seismic events:

$$\text{Log}_{10}(N) = a - bM \quad (1)$$

where  $N$  is the number of events with magnitude  $\geq M$ , and  $a$  and  $b$  are the parameters controlling the distribution. This relation corresponds to an exponential distribution with a single parameter, the  $b$ -value<sup>2</sup>. Earthquake kinematics and differential stress influence the  $b$ -value<sup>3–5</sup>. The  $b$ -value is a fundamental parameter for seismic hazard studies, particularly for probabilistic seismic hazard analyses, since it rules the percentage between small and large events<sup>6</sup>. Therefore, it is of primary importance to understand its variability across different portions of the Earth's crust and its correlations with other geophysical quantities. Studies on regional catalogs correlate the  $b$ -value with the earthquakes' depth: the shallower the event, larger the  $b$ -value<sup>7</sup>, apart from peculiar anomalies of high  $b$ -values in some subduction zones<sup>8</sup>. Regarding global catalogs, several studies have reported a  $b$ -value around 1.0 for regions undergoing strike-slip regime,  $b$ -value  $> 1$  in extensional settings, and  $b$ -value  $< 1$  in compressional ones<sup>9–11</sup>.

For assessing the relationship of the earthquake size distribution with the kinematics, two different strategies are generally used to quantify the  $b$ -value variations: a) analyzing the events according to the focal mechanisms; b) proceeding to a definition of a seismotectonic zonation and then analyzing the earthquakes of each zone. Both selection methods can potentially cause a mixture of geodynamics settings or faulting/tectonic styles. In the first case, a simplistic choice driven by focal mechanisms defining a normal-faulting earthquake class may mix two contrasting geodynamic settings: for example, seafloor spreading and back-arc extension. In the former, a new basaltic crust creates with the asthenosphere upwelling at the oceanic ridges in divergent plate boundaries. The extension in back-arc regions leads to the stretching and thinning of the continental or oceanic crust, forming basins filled with sediment and volcanic deposits. Notably, back-arc extension occurs near convergent boundaries behind the volcanic arc. Similarly, the thrust-faulting earthquake class mixes subduction-related and continental-convergent earthquakes. Though convergent settings characterize both, these geodynamic processes maintain substantial differences in fluid circulation, thermal state, and volcanic activity. These processes are expected to influence the  $b$ -value<sup>5</sup>.

In the second case, earthquakes are grouped using kinematic information from a regional seismotectonic model<sup>10,12</sup>. In this case, the accuracy of the  $b$ -values determination is mainly related to the correctness of the seismotectonic model. For example, a rough definition of a seafloor spreading seismotectonic zone overpopulates the extensional-earthquake group with the transform-fault earthquakes, resulting in a mixed faulting mechanism style, which is expected to influence the  $b$ -value. Consequently, the primary caution regarding this second approach is that there must be a reproducible and transparent definition of both the geographic boundaries of each seismogenic zone and its expected kinematics.

For this aim, geodetic measurements provide an unmatched, still underrated source of information to be used for an alternative selection method in the  $b$ -value estimation. The geodetic strain rates capture multiple rheological behaviors of the lithosphere and asthenosphere, spanning from the interseismic elastic deformation of rock volumes bordering active faults<sup>13</sup> to frictional sliding and viscoelastic relaxation induced by a strong earthquake<sup>14</sup> or deglaciation<sup>15</sup>. However, numerical models tuned on interseismic geodetic horizontal velocities and stress orientation data records have proved to adequately describe the long-term dynamics<sup>16–18</sup> and kinematics at the local scale<sup>19,20</sup>. In

this sense, crustal deformation measurements do not need any subjective choice for kinematics descriptions: the elastic rebound theory suggests that crustal volumes experience deformation in the interseismic phase, suddenly released as coseismic slip when frictional forces can no longer prevent the fault from slipping. Thus, the tectonic regime shown by geodetic strain rates can approximate the tectonic regime of earthquake strains and can be used to determine their kinematics quantified by the ratio of the two principal components of the geodetic horizontal strain rate tensor (see Methods). Furthermore, geodetic-derived strain rates are largely independent of the information in the seismic catalog and allow to delimit crustal volumes undergoing extension or compression, increasing the overall reliability of possible differences in the  $b$ -values<sup>21</sup>.

We propose an approach based on the 2D strain-rate tensor derived by the joint inversion of geodetic measurements and interpolated stress direction data (Fig. 1) to group earthquakes according to the interseismic deformation pattern of the volumes surrounding active faults. We test our approach for the Italian seismicity, representing an optimal target due to an adequate geodetic benchmark distribution and an excellent instrumental catalog. We intentionally delimited the southern boundary of our model to the parallel N39.6°, because geodetic data in the Calabria region are influenced by two conflicting processes: the extension of the forearc and the compression along the subduction plane. In this case, the 2D strain rate tensor cannot be used to determine the long-term one without inserting the active faults and their rates<sup>19</sup>.

## Results and discussion

**Calculation of compressional and extensional zones.** The interseismic strain rate tensor has been obtained by inverting geodetic horizontal velocities<sup>22</sup> and SHmax orientations<sup>23</sup>. Notably, the 2D strain rate tensor, with  $\dot{\epsilon}_{1h}$  and  $\dot{\epsilon}_{2h}$  being its principal horizontal values, allows us to determine any interseismic kinematics of the upper crust as long as data covers the study area, which is not the case for the Adriatic Sea region (see Methods). Consequently, the  $b$ -value variability of the strike-slip regimes (possibly including deep and/or offshore earthquakes<sup>24</sup>) can not be further investigated in our study area. These (excluded) events are probably due to bending in the dipping Adriatic slab, and, therefore, might have different physics and/or more complex stress regimes than shallow earthquakes. For the same reasons, we fixed the seismicity depth cutoff to 15 km to exclude deeper earthquakes with mixed regimes occurring onshore on the eastern side of the Apennines chain<sup>25</sup>. The earthquake catalog used to estimate the  $b$ -values is the 2005–2022 instrumental catalog (with homogenized moment magnitudes<sup>26</sup>).

We defined the compressional and extensional areas considering adequate coverage of geodetic and stress data records; then, we drew the borders at  $|\dot{\epsilon}_{1h}| \approx 6 \cdot 10^{-9} \text{yr}^{-1}$  (where  $\dot{\epsilon}_{1h} + \dot{\epsilon}_{2h} < 0$ ) and  $|\dot{\epsilon}_{2h}| \approx 12 \cdot 10^{-9} \text{yr}^{-1}$  (where  $\dot{\epsilon}_{1h} + \dot{\epsilon}_{2h} > 0$ ), respectively. The surface projections of both regions are shown in Fig. 2. Notably, the extensional region doesn't contain any volcanic area, which is expected to exhibit higher  $b$ -values.

**Comparison of expected and observed kinematics.** First, we inspected the literature and found several lines of evidence (paleotrenches, fault ribbon exposure rates, historical reports on past earthquakes' coseismic effects) unambiguously confirming our results for both extensional or compressional kinematics of the uppermost and frictional parts of the crust as shown in Fig. 2<sup>27,28</sup>. Then, we determined that the lateral variation of the strain rate tensor in Italy coherently reproduces the spatial distribution of earthquake kinematics reported for the past century

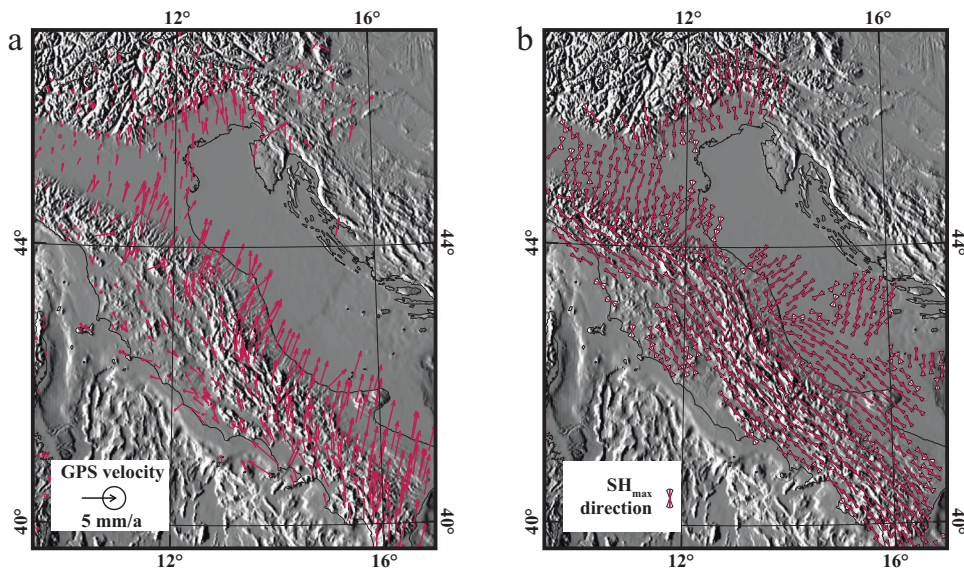


**Fig. 1 Geodetic and stress orientation data.** **a** Selected horizontal velocities from Serpelloni et al.<sup>22</sup>. **b**: Interpolated SHmax direction with the scheme of Carafa and Barba<sup>53</sup> and Carafa et al.<sup>54</sup> applied to the Mariucci and Montone<sup>23</sup> dataset.

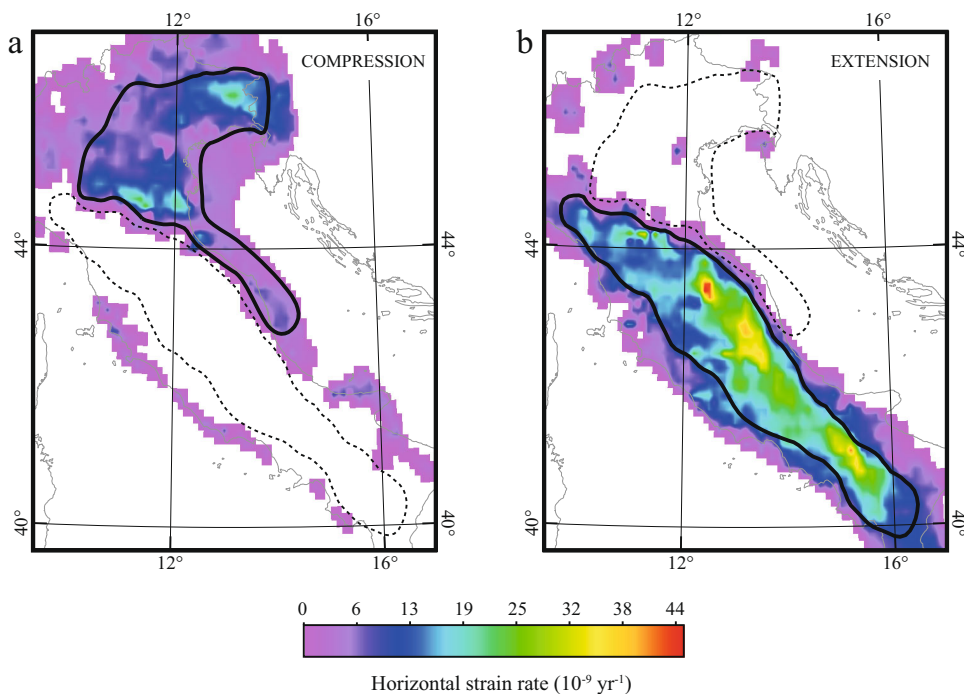


**Fig. 2 Greatest horizontal strain rate absolute value.** Map (split according to the expected regime, **a** compression, **b** extension) of the greatest absolute value of the horizontal strain rate.

in Mariucci and Montone<sup>23</sup> (see Methods). Finally, we explored whether the seismic moment release in each area is governed by a few earthquakes with different kinematics than the expected one (according to the geodetic data). To this end, we determined the ratio of the seismic moment of earthquakes with correct kinematics to the total seismic moment for both compressional and extensional areas. Kinematics of each earthquake was inferred by looking at the rake angles of the nodal planes. Table 1 shows the results of these tests: the ratio is about 0.96 for the compressional area, which raises to 0.99 for the extensional one (see Methods for details). We repeated the test for different borders of both regions to reject the possibility that the subjective choice of the bounding

strain-rate isoline is conditioning the final b-values (see Supplementary Material). In detail, we changed the strain-rate isoline to  $|\dot{\epsilon}_{1h}| \approx 9 \cdot 10^{-9} \text{yr}^{-1}$  for compression and  $|\dot{\epsilon}_{2h}| \approx 16 \cdot 10^{-9} \text{yr}^{-1}$  for extension without finding any appreciable difference in the seismic moment ratio (see Table 1).

All these tests confirm that our two zones correctly delimit extension and compression for Italy and, more in general, that the geodetically-derived definition of the expected kinematics of earthquakes is a reliable and useful approach.

The spatial pattern of expected kinematics is consistent with the seismotectonic zonation of Stucchi et al.<sup>29</sup> (hereafter St11). In contrast, it differs from Gulia and Wiemer<sup>10</sup> (hereafter GW10)

for the central-southern Apennines, where the authors draw a large transcurrent region based on the moment tensor of a few deep and easterly-located strike-slip earthquakes (Fig. 3). However, extensive paleo-seismological and Quaternary geology studies<sup>30–33</sup>, macroseismic data of historical earthquakes (1805 Matese earthquake,  $M_w = 6.8$ , see Guidoboni et al.<sup>34</sup> and references therein), and recent low<sup>35</sup> to moderate earthquakes (1984 Villetta Barrea earthquake,  $M_w = 5.8$ <sup>36,37</sup>) unambiguously indicate that the region upper crust is undergoing extension, as correctly depicted by data used in our work. This overall coherence with independent information suggests that the 2D-strain rate tensor derived from geodetic measurements should be incorporated into geophysical data to be considered for a reliable seismotectonic model.

**b-value estimation.** For both compressional and extensional regions, the b-value and its uncertainty are estimated by adequately considering the magnitude of completeness and the

possible short-term incompleteness after a main event in an earthquake sequence since it can strongly influence the resulting b-value<sup>38–40</sup>. In detail, we used different levels of completeness to also include the events in the early stage of aftershock sequences using a recent developed b-value estimation method<sup>41</sup>.

In Fig. 4, we show the results of the b-value estimations with different magnitudes of completeness thresholds for both the compressional and extensional regions. The statistical difference between the b-values estimated in the two crustal volumes is then tested using the Utsu test<sup>42</sup>. The b-value of the volume in extension is always significantly larger than in compression, confirming that the differential stress likely influences the earthquake size distribution. However, the b-values of both kinematic regimes are adjacent and defined in a relatively small range:  $0.92–1.16$ , considering the bounds of the 95% confidence intervals;  $0.98 \pm 0.03$  for compression (978 events from  $M_w 2.5$ ),  $1.13 \pm 0.01$  for extension (5077 events from  $M_w 2.5$ ).

Zone	Catalog	Ratio Moment Rake1	Ratio Moment Rake2
Compression (1)	RCMT	0.966	0.994
Extension (1)	RCMT	0.985	0.994
Compression (2)	RCMT	0.960	0.993
Extension (2)	RCMT	0.984	0.993
Compression (1)	Italian CMT	0.949	0.963
Extension (1)	Italian CMT	0.987	0.994
Compression (2)	Italian CMT	0.954	0.962
Extension (2)	Italian CMT	0.988	0.994

Ratio of the seismic moment in agreement with the model for the two areas according to the regional CMT (RCMT) and the Italian CMT catalogs (See Methods). Zone 1 refers to the areas of Fig. 2 (strain-rate isolate  $|\dot{\epsilon}_{1h}| \approx 6 \cdot 10^{-9} \text{yr}^{-1}$  - where  $\dot{\epsilon}_{1h} + \dot{\epsilon}_{2h} < 0$  - for compression and  $|\dot{\epsilon}_{2h}| \approx 12 \cdot 10^{-9} \text{yr}^{-1}$  - where  $\dot{\epsilon}_{1h} + \dot{\epsilon}_{2h} > 0$  - for extension); Zone 2 is obtained with strain-rate isolate  $|\dot{\epsilon}_{1h}| \approx 9 \cdot 10^{-9} \text{yr}^{-1}$  (where  $\dot{\epsilon}_{1h} + \dot{\epsilon}_{2h} < 0$ ) for compression and  $|\dot{\epsilon}_{2h}| \approx 16 \cdot 10^{-9} \text{yr}^{-1}$  (where  $\dot{\epsilon}_{1h} + \dot{\epsilon}_{2h} > 0$ ) for extension.

**Comparison with previous studies and test of our method.** The b-values we have determined are statistically different, but closer than expected or previously reported. As for the extensional zone, the b-value is similar to the one estimated by GW10<sup>10</sup> ( $1.09 \pm 0.02$  vs  $1.13 \pm 0.01$  for our analyses); however, it differs for the compressional region ( $0.75 \pm 0.02/0.78 \pm 0.02$  vs  $0.98 \pm 0.03$  for our analyses). Notably, their compressional zone is well aligned with known active seismogenic sources<sup>43</sup> located in the northeast of Italy; instead, our compressional area is bigger (more than double the size of GW10<sup>10</sup>). These differences became smaller if we applied our method and our catalog to the GW10<sup>10</sup> zones (Fig. S1 and Table S1 in Supplementary Information), suggesting that the discrepancies in the aforementioned estimations could be due to a different magnitude scale adopted (Mw in our case vs ML in the original GW10<sup>10</sup> estimation).

As for the b-values determined by St11<sup>31</sup>, our extensional area overlies on nine of their zones, for which a b-value variability between 0.74 and 1.96 is reported ( $1.13 \pm 0.01$  in our case). Similarly, our compressional area overlaps four zones of St11<sup>31</sup>,

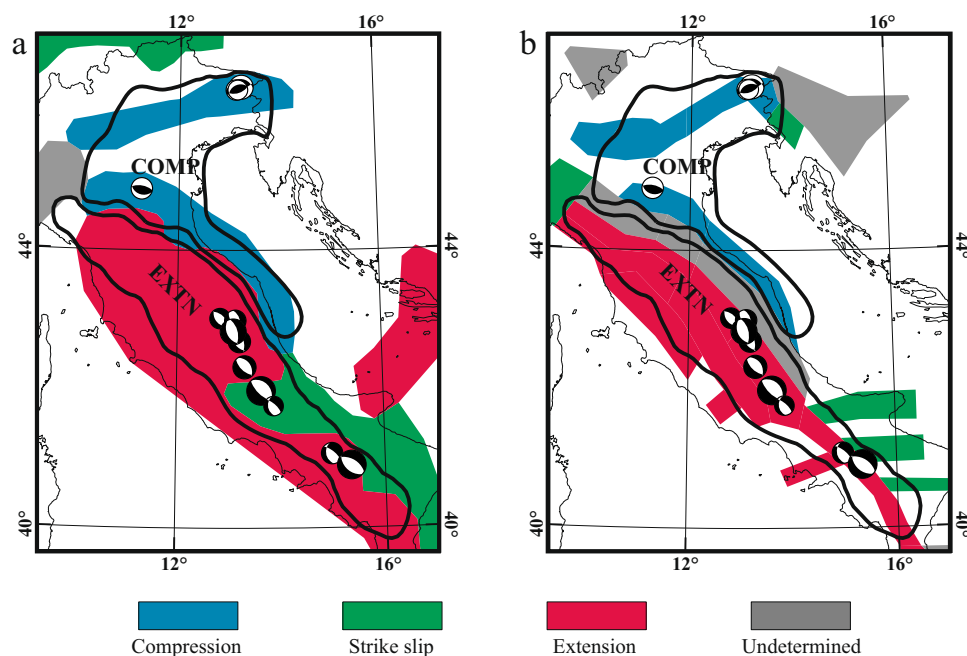


**Fig. 3** Comparison of expected kinematics among different zonations. The borders of the two zones determined in this work are shown in both pictures (COMP: compressional region; EXTN: extensional region). **a** The colors refer to the expected kinematics from GW10<sup>10</sup>; **b**, the kinematics from the zonation of St11<sup>31</sup> are reported. Focal mechanisms for earthquakes  $M_w > 5.8$  are shown<sup>23</sup>.

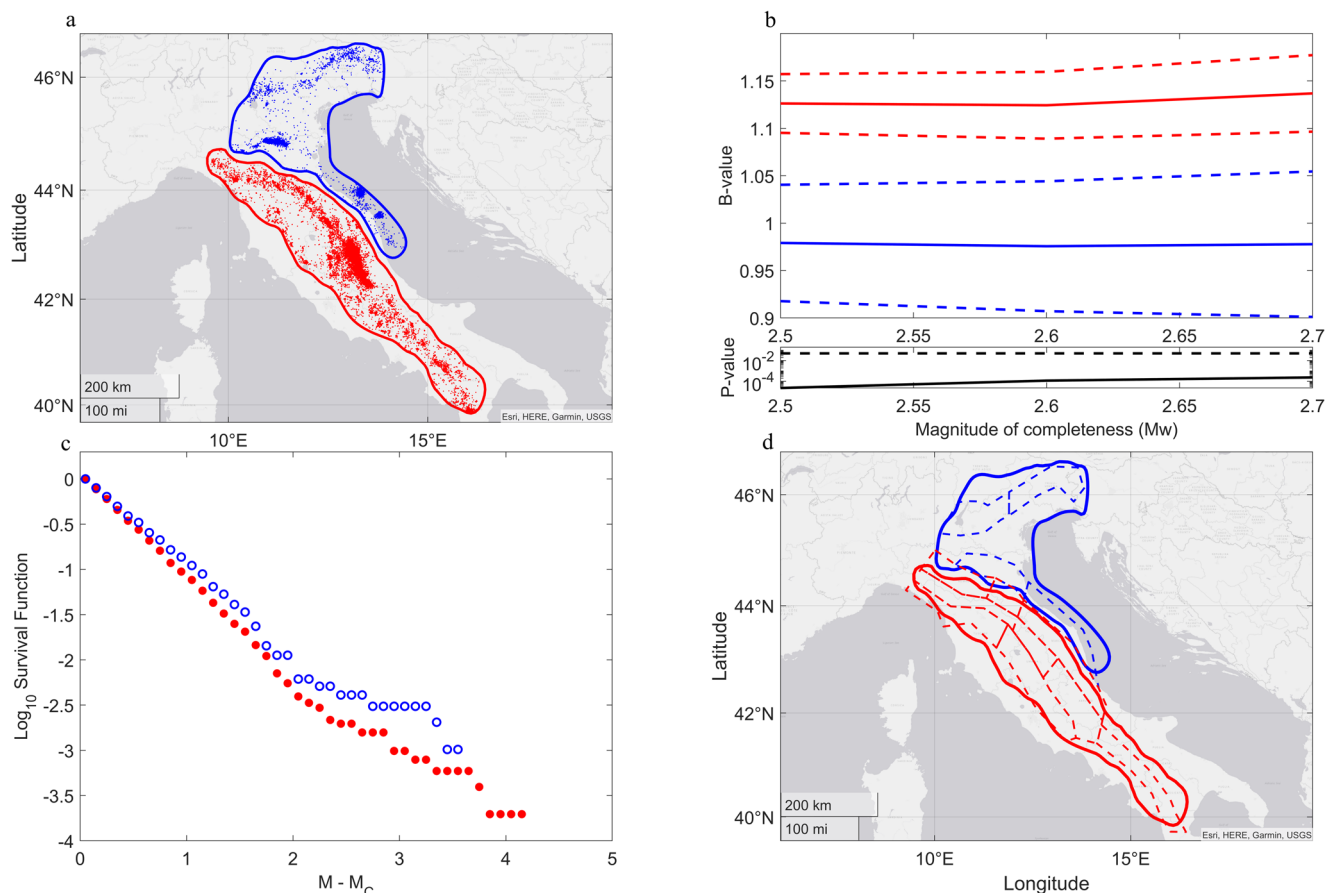


**Fig. 4 B-value estimation and comparison.** **a** Extensional (red) and compressional (blue) zones, with the epicenters of events used for the b-value estimation. **b**: b-values (solid lines) for the extensional (red) and compressional (blue) zones, along with their 95% confidence intervals (dashed lines) for different magnitudes of completeness, from 2.5 to 2.7 (these thresholds are increased by 1.0 during short-term aftershocks incompleteness periods, see Methods for details); lower part of the panel represents the  $p$  value of the Utsu test (solid black line) in a log<sub>10</sub> scale, the dashed line represents the 0.05  $p$  value threshold. **c** survival function of the magnitude frequency distributions in a log<sub>10</sub> scale (red dots for extension and blue circles for compression since we used different levels of completeness in the b-value estimation, this X-axis shows  $M - M_c$  instead of  $M^{63}$ ). **d**: Zones of the St11<sup>31</sup> zonation (dashed polygons), colored according to the kinematics of the zones determined in our work (red for extension and blue for compression).

characterized by a larger range of 1.04–1.35 than our estimates ( $0.98 \pm 0.03$ ). These differences remain large also if we apply our method and our catalog to the St11<sup>31</sup> zones (Fig. S1 and Table S1 in Supplementary Information).

Hence, is the higher b-value variability of St11<sup>31</sup> due to the limited number of earthquakes falling in the zones, or is it due to local earthquake characteristics (host rocks, thermal conditions, rheology parameters) in a homogenous tectonic regime? We performed a simple but rigorous two-steps experiment to investigate this point.

In the first step, we split the earthquake catalog into learning and testing datasets (25–75%, respectively). Using the learning dataset, we estimated the b-value for the compressional and extensional areas determined in our work. Similarly, we calculated the b-value for 13 zones (9 zones for the extensional setting and four zones for the compressional setting) of St11<sup>31</sup> overlapping our extensional and compressional zones. Therefore, using the same dataset, we have determined 13 different b-values for St11<sup>31</sup> zones and two b-values for the extensional and compressional areas determined with geodetic data. In the second step, we used the testing dataset to check whether the magnitude distribution in the 13 zones of St11<sup>31</sup> is better described by their local b-value determined in the first step or with the b-value estimated for the larger zones determined in our work with the

corresponding tectonic regime. As a comparison metric, we adopt the Bayes Factor<sup>44</sup>, already used in seismological comparison studies<sup>45,46</sup>. We found that two b-values of compressional and extensional areas better describe the magnitude distribution of the testing dataset in the 13 zones of St11<sup>31</sup> than the 13 b-values determined with the learning dataset (Table 2, see Methods for details).

## Conclusions

Interseismic geodetic strain rates and horizontal stress directions can be used to define the extensional and compressional zones in the Italian region. The resulting b-value of the Gutenberg-Richter law in these zones is significantly larger in the extensional setting than in the compressional one, although these differences are much smaller than previously reported. We finally verify that our zones and their small b-value differences are coherent with observed seismicity.

Consequently, the large b-value differences seen in previous studies can appear as artifacts when the spatial zones of a seismotectonic model are too small; the undersampling of the earthquake size distribution affects the computation, resulting in an overdispersed representation of b-values. Similarly, some b-value variations of adjacent small regions are wrongly

**Table 2 Models comparison results.**

Zone type	Percentage Learning - Testing	Bayes Factor (log <sub>e</sub> scale)	Bayes Factor Interpretation
1	20–80%	9.49	Decisive Evidence in favor of this study
1	25–75%	14.54	Decisive Evidence in favor of this study
1	33–67%	2.97	Strong Evidence in favor of this study
2	20–80%	9.24	Decisive Evidence in favor of this study
2	25–75%	13.34	Decisive Evidence in favor of this study
2	33–67%	3.14	Strong Evidence in favor of this study

Bayes Factor values and their interpretation (according to Kass and Raftery<sup>44</sup>) for different percentages of learning and testing datasets; see Table 1 for the definition of Zone type 1 and 2.

attributed to different kinematics when using subjective and sharp boundaries, but they average out when using independent and reproducible methods such as the geodetically derived strain rates. It follows that some large spatial b-value fluctuations are probably due to intrinsic stochastic variability more than a physical feature of the seismicity. These principles of interpreting apparent b-value variations (governed by undersampling more than by physical processes) could be valid for other applications by using an appropriate and meaningful resolution/selection<sup>46–50</sup>.

Some direct implications follow from our work for the probabilistic seismic hazard analysis. Before using b-values for earthquake forecasting, careful inspection of their variations is required because it could mainly derive from an excessive splitting of the study area in small (as in the case of Stucchi et al.<sup>29</sup>) and/or kinematically wrong zones (as in the case of some zones drew in Gulia and Wiemer<sup>10</sup>). At least for the Italian peninsula, where geodetic data density is adequate, using simple, reproducible (and falsifiable) rules based on the 2D strain rate tensor reduces the difference in b-values between extensional and compressional settings. Clearly, in global seismic catalogs that also include oceanic ridges (for extension) and subduction zones (for compression), these b-value differences can be much larger.

## Methods

**Definition of compressional and extensional domains by inverting GNSS-derived horizontal velocities and interpolated SHmax directions.** The diagonalization of a  $2 \times 2$  geodetically-derived horizontal-plane strain-rate tensor gives the principal horizontal values  $\dot{\epsilon}_{1h}$  (more negative or compressional) and  $\dot{\epsilon}_{2h}$  (more positive or extensional) and their associated principal axis directions. If we plot both values in a cartesian plane of the horizontal principal strain rates, it is always possible to define the kinematics of a given 2D geodetically-derived strain rate tensor. By definition of  $\dot{\epsilon}_{1h}$  and  $\dot{\epsilon}_{2h}$ , only the area above the bisector of the 1st–3rd quadrants can be populated. In detail, the first quadrant unambiguously defines a normal-faulting tectonic regime, whereas the third quadrant delimitates the thrust-faulting one. The transition from transtension to pure strike-slip to transpression can be identified in the second quadrant, moving counterclockwise<sup>51</sup>.

The spatial distribution of the 2D strain rates is obtained with the NeoKinema code<sup>52</sup>, which has repeatedly been proven to be successful in modeling the active tectonics of the central Mediterranean<sup>13,19</sup>. The model strain rates are obtained by simultaneously inverting the GPS velocities of Serpelloni et al.<sup>22</sup> and interpolated SHmax directions of Mariucci and Montone<sup>23</sup> on a ~15-km laterally-spaced 2-D finite element grid. The SHmax directions are interpolated with the procedure described in Carafa and Barba<sup>53</sup> and Carafa et al.<sup>54</sup>. The general objective function of our inversion with the NeoKinema code is:

$$\Pi \equiv -(\vec{p} - \vec{r})^T \left[ \tilde{C}_{GPS}^{-1} \right] (\vec{p} - \vec{r}) - \frac{1}{A_0} \sum_{n=1}^3 \iint_{area} \frac{(p_n - r_n)^2}{\sigma_n^2} da \quad (2)$$

where  $\vec{p}$  is the vector of (scalar) model predictions, and  $\vec{r}$  is the vector of (scalar) data; and  $n = 1, 2, 3$  enumerates 3 target rates associated with three independent functionals of permanent strain-rate at each continuum point. Although the kinematics of both compressional and extensional remain stable for a large range of the dimensional parameter  $A_0$ , we set it to  $A_0 = 1 \cdot 10^8 \text{m}^2$ . In this case, the error (L1 norm) of the model predictions is 0.34 mm/yr relative to the geodetic data and  $10^\circ$  relative to the interpolated stress directions.

The target velocities derived from geodetic data are included in the first term of the objective function. In contrast, the second term contains the targets derived from interpolated stress-direction data and the stiff-continuum assumption. This second term describes the size and orientation of distributed permanent deformation rate tensors for each finite element. The elastic rebound theory suggests that the strain rate is high near active faults or plate boundaries and tends to zero in stable plate interiors. An appropriate formalism for this “microplate assumption” is to assign a zero target strain rate with a statistical uncertainty  $\mu$ <sup>51,55</sup> that can be seen as the regional RMS of the interseismic strain rate. We determined  $\mu$  by iteration: we choose a starting  $\mu$  value as an input parameter in Eq. (2) and then compare it to the average interseismic strain rate from the model output. For our work, the value  $\mu = 6.56 \cdot 10^{-9} \text{yr}^{-1}$  minimizes the difference between the model input and output and is selected as optimal.

The resulting strain rate map (Fig. 2) derived from GNSS horizontal velocities shows two well-delimited and divided regions undergoing compression/transpression (Southern Alps) and extension/transension (Apennines). Notably, the extensional region doesn't contain any volcanic area, which is expected to exhibit higher b-values.

As for the transition in the second quadrant from extension/transension to pure strike-slip to compression/transpression, we derived it from the ratio of  $\dot{\epsilon}_{1h}$  and  $\dot{\epsilon}_{2h}$  resulting from the kinematic inversion. When the principal values differ in sign, we can derive that the kinematic of a 2D strain-rate tensor is transensional (thus undergoing extension) if  $\dot{\epsilon}_{2h} > -(1 - k_1) \cdot \dot{\epsilon}_{1h}$ ; transpressional (compression) if  $\dot{\epsilon}_{2h} < -\frac{1}{(1 - k_1)} \cdot \dot{\epsilon}_{1h}$ , strike-slip otherwise. In Fig. 5, we show that for our study area, the definition of transtension and transpression in the second quadrant resulting from  $k_1 = 0.25$  is consistent with the observed principal components of the 2D strain rate tensor for finite elements falling in both areas. For the extensional area, this observation is consistent with  $\dot{\epsilon}_{1h}$  being negative (though marginal) and linked to the far-field Africa-Eurasia convergence<sup>17</sup>. Similarly, in the Southern Alps, the clockwise rotation of Adria relative to the Eurasia plate determines a lateral transition from pure thrust earthquakes to transpression to strike-slip ones<sup>56</sup>, thus  $\dot{\epsilon}_{2h}$  being positive though marginal.

To confirm the coherence between interseismic strain rates and earthquake kinematics, we used the IPSI focal mechanisms<sup>23</sup> for

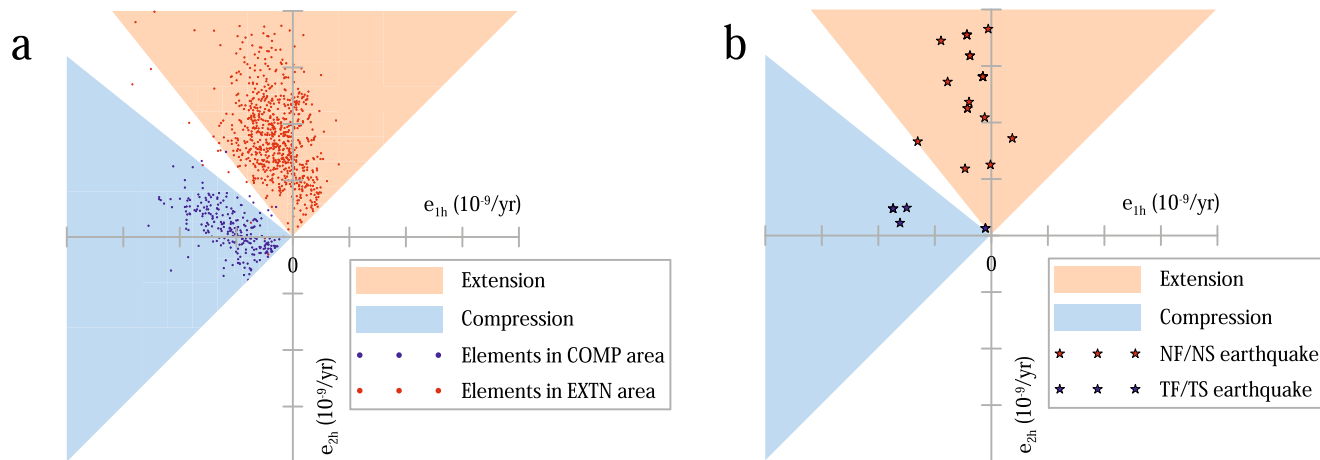


**Fig. 5 Analysis of horizontal strain rate principal values.** **a** Horizontal strain rate principal values ( $\dot{\epsilon}_{1h}$  and  $\dot{\epsilon}_{2h}$ ) for finite elements falling in extensional and compressional areas versus the tectonic regime definition resulting from  $k_1 = 0.25$ . **b** IPSE earthquake kinematics versus the tectonic regime definition resulting from  $k_1 = 0.25$ .

earthquakes that occurred after 1900 AD, which are already grouped according to their tectonic regime. In the cartesian plane of the horizontal strain rates, we plotted each IPSE earthquake labeled with “TF” or “TS” and “NF” or “NS” and that fell in our compressional and extensional regions. The earthquake coordinates in the strain-rate cartesian plane are the principal values  $\dot{\epsilon}_{1h}$  and  $\dot{\epsilon}_{2h}$  of the element where the earthquake falls. The excellent overlap in the cartesian plane of each earthquake point with its expected tectonic regime resulting from  $k_1 = 0.25$  confirms our basic assumption that interseismic strain rate can be used as a good proxy for the earthquake kinematics (Fig. 5).

**Determining the ratio between the correctly determined and the total seismic moment for each area.** We checked the consistency between our compressional and extensional areas using independent observations. These observations are the earthquakes of two catalogs: the regional CMT catalog<sup>57</sup> (1997–2022), and the Italian CMT catalog<sup>58</sup> (1976–2015).

For both catalogs, we selected all earthquakes falling in these two areas and calculated the ratio of the seismic moment between the earthquakes with matched kinematics with the total one. To select the correct kinematics, we used the rake angle of the first and the second nodal planes, available in the catalogs. The moment magnitudes of the catalogs are converted into seismic moments using the classical Kanamori equation. The resulting values are illustrated in Table 1.

**Magnitude of completeness.** Estimating the magnitude of completeness is a fundamental step in correctly analyzing the b-value. Here, we used the approach of Herrmann and Marzocchi<sup>38</sup>, based on the Lilliefors test. We consider the catalog complete above a threshold magnitude if it follows an exponential distribution, as the Gutenberg-Richter law states. We apply this method to the Italian instrumental HORUS catalog from 2005-4-16 to 2022-12-31<sup>26</sup> (from the 16th of April 2005, there was a change in the Italian seismic network and increased data availability). We consider the events inside our two areas, with a maximum depth of 30 km. This depth is larger than the one finally used for the b-value estimation, 15 km, but since we also investigate this second threshold of depth in a sensitivity analysis we need to set a reliable completeness until 30 km. The resulting magnitude of completeness is Mw 1.8. We then carefully check the short-term aftershocks incompleteness problem (STAI effect<sup>40</sup>); for each earthquake with a magnitude larger than Mw 5.5, we consider

that in the following 3 days, the completeness threshold is incremented by 1 (i.e., from 1.8 to 2.8). This increment should remove the STAI effect without losing all the events of the aftershock sequences. However, recent works suggest that modern statistical methods for the completeness estimation could also underestimate the real completeness thresholds<sup>39,59</sup>. Zhuang et al.<sup>60</sup> suggest looking to the incremental number vs magnitude plot to find possible incompleteness in the catalog: the incomplete parts are indicated by white empty spaces in the lower part of the plot or vertical alignment of dots. Taroni et al. (2021)<sup>61</sup> showed that this method is also effective in the catalogs with a variable magnitude of completeness (e.g., during STAI periods), if Magnitude -  $M_c$  (i.e., the magnitude of the earthquake minus the corresponding magnitude of completeness) is plotted instead of the magnitude. In Fig. 6 these plots are shown: some incompleteness is present in the case of  $M_c = 1.8$  (panel a) and  $M_c = 1.8$  with an increase of 1.0 during STAI periods (panel b). Thus, we decided to use the value of  $M_c = 2.5$ . This value also has an operational meaning because it matches the communication threshold of the seismic surveillance room at INGV with the Italian Department of Civil Protection<sup>62</sup>. Thus, by definition,  $M_c = 2.5$  ensures the detection of all seismic events in the Italian territory. Figure 6 (panel c) demonstrates that this 2.5 threshold shows no suspect incompleteness period.

**B-value estimation and test.** After the computation of the completeness, we selected the events in the extensional and compressional regions, with a maximum depth of 15 km (see main text for this choice of depth). Since we used different completeness thresholds to account for the STAI effect, we estimate the b-value ( $\hat{b}$ ) using the Taroni<sup>41</sup> approach:

$$\hat{b} = \frac{\frac{N-1}{N}}{\log(10) \left[ \frac{\sum_{i=1}^N (M_i - M_i^c)}{N} + \frac{\Delta M}{2} \right]} \quad (3)$$

Where  $N$  is the total number of events above the completeness,  $M_i$  is the magnitude of the  $i$ -th event,  $M_i^c$  is the completeness magnitude at the time of the  $i$ -th event, and  $\Delta M$  is the magnitude binning. This equation also contains the correction for an unbiased estimation (the  $\frac{N-1}{N}$  in the numerator) and the correction for the magnitude binning (the  $\frac{\Delta M}{2}$  in the denominator). We computed the 95% confidence interval using the normal approximation  $[\hat{b} - 1.96\hat{\sigma}, \hat{b} + 1.96\hat{\sigma}]$ , where  $\hat{b}$  and  $\hat{\sigma}$  (sigma) are estimated with the Taroni (2021)<sup>41</sup> approach. To test the

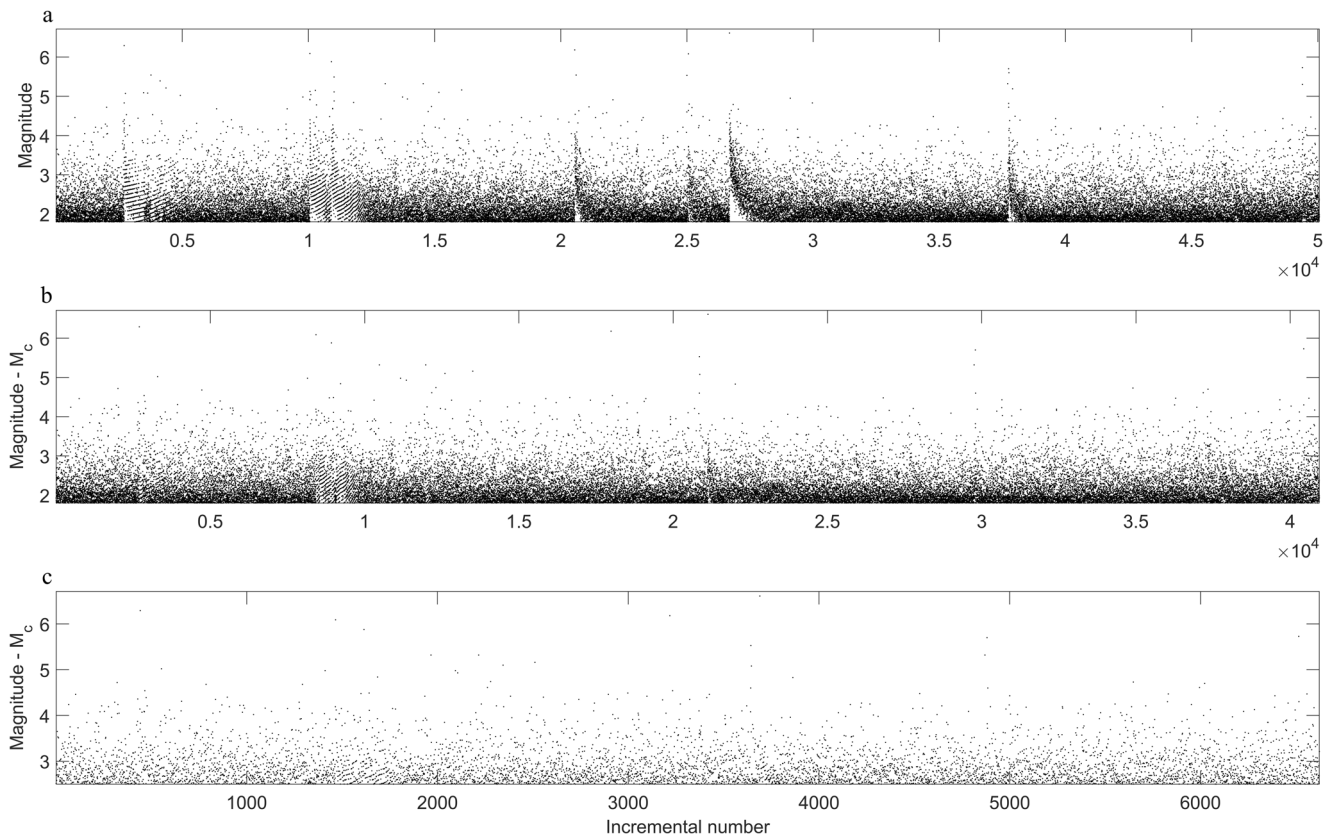


**Fig. 6 Temporal variation of the completeness magnitude.** **a** Incremental number vs magnitude plot for the earthquakes in the catalog with magnitude  $\geq 1.8$ . **b** Incremental number vs Magnitude -  $M_c$  plot for the earthquakes in the catalog with magnitude  $\geq 1.8$ , with  $M_c$  increased by 1.0 during STAI periods. **c** Incremental number vs Magnitude -  $M_c$  plot for the earthquakes in the catalog with magnitude  $\geq 2.5$ , with  $M_c$  increased by 1.0 during STAI periods.

significance of the b-value difference, we used the classical Utsu test<sup>42</sup>, which is still valid if the b-value is estimated with the Taroni (2021)<sup>41</sup> approach. The Utsu test uses the information on the number of events  $N$  and the estimated b-value  $\hat{b}$  in each of the two sets of observations. The null hypothesis of this test is an equal distribution for the two sets of observations: in the case of a low p-value of the test (e.g., p-value  $< 0.05$ ), the null hypothesis must be rejected and the two b-values can be considered significantly different. To avoid possible bias in the estimation due to undetected incompleteness, we also performed b-value estimation and test for higher thresholds of completeness (until Mw 2.7, and in this case, the completeness after strong earthquakes is Mw 3.7, i.e.,  $2.7 + 1$ ). A straightforward sensitivity test with depth cutoff set to 25 km instead of 15 km obtained the same results, implying a marginal effect of depth on b-value estimation in this analysis (Fig. S2 in Supplementary Information). Very similar results are also obtained using Type 2 of compressional and extensional zones (see Table 1 for the definition of these zones, and Fig. S3 in Supplementary Information for the relative results).

**Two-steps experiment on b-value comparison between different seismotectonic models.** Here, we better explain our comparison check between the Stucchi et al.<sup>29</sup> zonation approach and our model. We split the catalog into a learning dataset (20–25–33% of the data) and a testing dataset (80–75–67% of the data). Note that to have a meaningful experiment the testing dataset must contain more events than the learning dataset. To avoid possible temporal bias for the two subsets, we selected the learning dataset uniformly with respect to time (in the case of 25–75%, 1st, 5th, 9th, 13th, etc. events) and the same for the testing dataset (2nd, 3rd, 4th, 6th, 7th, etc. events). We used the events falling in the intersection of our two

zones and the Stucchi et al.<sup>29</sup> zonation (4 zones for our compressional region and 9 zones for our extensional region). We computed the b-value for each of the 13 zones and for our two larger regions; then, we used the events of the testing catalog inside each of the 13 zones to check if these events are better modeled by the local b-value of their own zone or by the global b-value of our two large regions. We used the Bayes Factor<sup>44</sup>, a simple, robust, and popular approach already used in the b-value comparison<sup>41</sup>. By aggregating the comparisons for all 13 zones, we obtain decisive/strong evidence favoring our approach (Table 2).

#### Data availability

The dataset used in this paper is freely available at: <https://zenodo.org/record/8391652>

#### Code availability

The code used in this paper is freely available at: <https://zenodo.org/record/8391652>

Received: 7 April 2023; Accepted: 19 October 2023;

Published online: 31 October 2023

#### References

1. Gutenberg, B. & Richter, C. F. Frequency of earthquakes in California\*. *Bull. Seismol. Soc. Am.* **34**, 185–188 (1944).
2. Aki, K. Maximum likelihood estimate of b in the formula  $\log N = a - bM$  and its confidence limits. *Bull. Earthq. Res. Inst. (Tokyo)*, **43** 237–239 (1965).
3. Petrucci, A., Vannucci, G., Lolli, B. & Gasperini, P. Harmonic fluctuation of the slope of the frequency-magnitude distribution (b-value) as a function of the angle of rake. *Bull. Seismol. Soc. Am.* **108**, 1864–1876 (2018).



4. Scholz, C. H. The frequency-magnitude relation of microfracturing in rock and its relation to earthquakes. *Bull. Seismol. Soc. Am.* **58**, 399–415 (1968).
5. Scholz, C. H. On the stress dependence of the earthquake b-value. *Geophys. Res. Lett.* **42**, 1399–1402 (2015).
6. Gerstenberger, M. C. et al. Probabilistic seismic hazard analysis at regional and national scales: state of the art and future challenges. *Rev. Geophys.* **58**, e2019RG000653 (2020).
7. Gerstenberger, M., Wiemer, S. & Giardini, D. A systematic test of the hypothesis that the b-value varies with depth in California. *Geophys. Res. Lett.* **28**, 57–60 (2001).
8. Wiemer, S. & Benoit, J. P. Mapping the b-value anomaly at 100 km depth in the Alaska and New Zealand subduction zones. *Geophys. Res. Lett.* **23**, 1557–1560 (1996).
9. Schorlemmer, D., Wiemer, S. & Wyss, M. Variations in earthquake-size distribution across different stress regimes. *Nature* **437**, 539–542 (2005).
10. Gulia, L. & Wiemer, S. The influence of tectonic regimes on the earthquake size distribution: a case study for Italy. *Geophys. Res. Lett.* **37**, <https://doi.org/10.1029/2010gl043066> (2010).
11. Petrucci, A. et al. The influence of faulting style on the size-distribution of global earthquakes. *Earth Planet. Sci. Lett.* **527**, 115791 (2019).
12. Kagan, Y. Y., Bird, P. & Jackson, D. D. Earthquake patterns in diverse tectonic zones of the globe. *Pure Appl. Geophys.* **167**, 721–741 (2010).
13. Carafa, M. M. C. et al. Partitioning the ongoing extension of the central Apennines (Italy): fault slip rates and bulk deformation rates from geodetic and stress data. *J. Geophys. Res.: Solid Earth*, <https://doi.org/10.1029/2019JB018956> (2020).
14. Hu, Y., Burgmann, R., Uchida, N., Banerjee, P. & Freymueller, J. T. Stress-driven relaxation of heterogeneous upper mantle and time-dependent afterslip following the 2011 Tohoku earthquake. *J. Geophys. Res.-Sol. Ea* **121**, 385–411 (2016).
15. Kierulf, H. P. et al. Time-varying uplift in Svalbard—an effect of glacial changes. *Geophys. J. Int.* **231**, 1518–1534 (2022).
16. Faccenna, C. & Becker, T. W. Shaping mobile belts by small-scale convection. *Nature* **465**, 602–605 (2010).
17. Carafa, M., Barba, S. & Bird, P. Neotectonics and long-term seismicity in Europe and the Mediterranean region. *J. Geophys. Res.-Sol. Ea* **120**, 5311–5342 (2015).
18. Neres, M. et al. Lithospheric deformation in the Africa-Iberia plate boundary: improved neotectonic modeling testing a basal-driven Alboran plate. *J. Geophys. Res.-Sol. Ea* **121**, 6566–6596 (2016).
19. Carafa, M. M. C., Kastelic, V., Bird, P., Maesano, F. E. & Valensise, G. A “Geodetic Gap” in the Calabrian arc: evidence for a locked subduction megathrust? *Geophys. Res. Lett.* **45**, 1794–1804 (2018).
20. Albano, M. et al. Three-dimensional numerical simulation of the interseismic and coseismic phases associated with the 6 April 2009, Mw 6.3 L’Aquila earthquake (Central Italy). *Tectonophysics* **798**, 228685 (2021).
21. Aguilera Bustos, J. P., Taroni, M. & Adam, L. A robust statistical framework to properly test the spatiotemporal variations of the b-value: an application to the geothermal and volcanic zones of the Nevado del Ruiz Volcano. *Seismol. Res. Lett.* **93**, 2793–2803 (2022).
22. Serpelloni, E. et al. Surface velocities and strain-rates in the Euro-Mediterranean region from massive GPS data processing. *Front. Earth Sci.* **10**, <https://doi.org/10.3389/feart.2022.907897> (2022).
23. Mariucci, M. T. & Montone, P. Database of Italian present-day stress indicators, IPSI 1.4. *Sci. Data* **7**, 298 (2020).
24. Di Bucci, D. & Angeloni, P. Adria seismicity and seismotectonics: review and critical discussion. *Mar. Petrol. Geol.* **42**, 182–190 (2013).
25. de Nardis, R. et al. Lithospheric double shear zone unveiled by microseismicity in a region of slow deformation. *Sci. Rep.* **12**, 21066 (2022).
26. Lolli, B., Randazzo, D., Vannucci, G. & Gasperini, P. The Homogenized Instrumental Seismic Catalog (HORUS) of Italy from 1960 to present. *Seismol. Res. Lett.* **91**, 3208–3222 (2020).
27. Carafa, M. M. C., Di Naccio, D., Di Lorenzo, C., Kastelic, V. & Bird, P. A meta-analysis of fault slip rates across the central apennines. *J. Geophys. Res.-Sol. Ea* **127**, e2021JB023252 (2022).
28. Poli, M. E. & Zanferrari, A. The seismogenic sources of the 1976 Friuli earthquakes: a new seismotectonic model for the Friuli area. *Bollettino Di Geofisica Teorica Ed Applicata* **59**, 463–480 (2018).
29. Stucchi, M. et al. Seismic Hazard Assessment (2003–2009) for the Italian building code. *Bull. Seismol. Soc. Am.* **101**, 1885–1911 (2011).
30. Ferrarini, F. et al. Segmentation pattern and structural complexities in seismogenic extensional settings: the North Matese Fault System (Central Italy). *J. Struct. Geol.* **95**, 93–112 (2017).
31. Esposito, A. et al. Concurrent deformation processes in the Matese massif area (Central-Southern Apennines, Italy). *Tectonophysics* **774**, 228234 (2020).
32. Ferranti, L., Milano, G., Burrato, P., Palano, M. & Cannavo, F. The seismogenic structure of the 2013–2014 Matese seismic sequence, Southern Italy: implication for the geometry of the Apennines active extensional belt. *Geophys. J. Int.* **201**, 823–837 (2015).
33. Boncio, P., Dichiarante, A. M., Auciello, E., Saroli, M. & Stoppa, F. Normal faulting along the western side of the Matese Mountains: implications for active tectonics in the Central Apennines (Italy). *J. Struct. Geol.* **82**, 16–36 (2016).
34. Guidoboni, E. et al. CFTI5Med, the new release of the catalogue of strong earthquakes in Italy and in the Mediterranean area. *Sci. Data* **6**, 80 (2019).
35. Frepoli, A. et al. Seismic sequences and swarms in the Latium-Abruzzo-Molise Apennines (central Italy): new observations and analysis from a dense monitoring of the recent activity. *Tectonophysics* **712–713**, 312–329 (2017).
36. Westaway, R., Gawthorpe, R. & Tozzi, M. Seismological and field observations of the 1984 Lazio-Abruzzo earthquakes: implications for the active tectonics of Italy. *Geophys. J. Int.* **98**, 489–514 (1989).
37. Pace, B., Boncio, P. & Lavecchia, G. The 1984 Abruzzo earthquake (Italy): an example of seismogenic process controlled by interaction between differently oriented synkinematic faults. *Tectonophysics* **350**, 237–254 (2002).
38. Herrmann, M. & Marzocchi, W. Inconsistencies and lurking pitfalls in the magnitude–frequency distribution of high-resolution earthquake catalogs. *Seismol. Res. Lett.* **92**, 909–922 (2020).
39. Marzocchi, W., Spassiani, I., Stallone, A. & Taroni, M. How to be fooled searching for significant variations of the b-value. *Geophys. J. Int.* **220**, 1845–1856 (2020).
40. Lolli, B. & Gasperini, P. Comparing different models of aftershock rate decay: the role of catalog incompleteness in the first times after main shock. *Tectonophysics* **423**, 43–59 (2006).
41. Taroni, M. Back to the future: old methods for new estimation and test of the Gutenberg–Richter b-value for catalogues with variable completeness. *Geophys. J. Int.* **224**, 337–339 (2021).
42. Utsu, T. A statistical significance test of the difference in b-value between two earthquake groups. *J. Phys. Earth* **14**, 37–40 (1966).
43. Galadini, F., Poli, M. E. & Zanferrari, A. Seismogenic sources potentially responsible for earthquakes with  $M \geq 6$  in the eastern Southern Alps (Thiene–Udine sector, NE Italy). *Geophys. J.*, 739–762, <https://doi.org/10.1111/j.1365-246X.2005.02571.x> (2005).
44. Kass, R. E. & Raftery, A. E. Bayes factors. *J. Am. Stat. Assoc.* **90**, 773–795 (1995).
45. Marzocchi, W., Zechar, J. D. & Jordan, T. H. Bayesian forecast evaluation and ensemble earthquake forecasting. *Bull. Seismol. Soc. Am.* **102**, 2574–2584 (2012).
46. Taroni, M., Zhuang, J. C. & Marzocchi, W. High-definition mapping of the gutenbergrichter b-value and its relevance: a case study in Italy. *Seismol. Res. Lett.* **92**, 3778–3784 (2021).
47. Godano, C., Convertito, V., Pino, N. A. & Tramelli, A. An automated method for mapping independent spatial b-values. *Earth Space Sci.* **9**, e2021EA002205 (2022).
48. Herrmann, M., Piegari, E. & Marzocchi, W. Revealing the spatiotemporal complexity of the magnitude distribution and b-value during an earthquake sequence. *Nat. Commun.* **13**, 5087 (2022).
49. Morales-Yanez, C., Bustamante, L., Benavente, R., Sippl, C. & Moreno, M. B-value variations in the Central Chile seismic gap assessed by a Bayesian transdimensional approach. *Sci. Rep.* **12**, 21710 (2022).
50. Roberts, N. S., Bell, A. F. & Main, I. G. Mode switching in volcanic seismicity: El Hierro 2011–2013. *Geophys. Res. Lett.* **43**, 4288–4296 (2016).
51. Bird, P. Long-term fault slip rates, distributed deformation rates, and forecast of seismicity in the western United States from joint fitting of community geologic, geodetic, and stress direction data sets. *J. Geophys. Res. Solid Earth* **114**, <https://doi.org/10.1029/2009jb006317> (2009).
52. Bird, P. & Carafa, M. M. C. Improving deformation models by discounting transient signals in geodetic data: 1. Concept and synthetic examples. *J. Geophys. Res. Solid Earth* **121**, 5538–5556 (2016).
53. Carafa, M. M. C. & Barba, S. The stress field in Europe: optimal orientations with confidence limits. *Geophys. J. Int.* **193**, 531–548 (2013).
54. Carafa, M. M. C., Tarabusi, G. & Kastelic, V. SHINE: Web application for determining the horizontal stress orientation. *Comput. Geosci.* **74**, 39–49 (2015).
55. Carafa, M. M. C. & Bird, P. Improving deformation models by discounting transient signals in geodetic data: 2. Geodetic data, stress directions, and long-term strain rates in Italy. *J. Geophys. Res. Solid Earth* **121**, 5557–5575 (2016).
56. Kastelic, V., Vrabec, M., Cunningham, D. & Gosar, A. Neo-Alpine structural evolution and present-day tectonic activity of the eastern Southern Alps: the case of the Ravne Fault, NW Slovenia. *J. Struct. Geol.* **30**, 963–975 (2008).
57. Pondrelli, S. European-Mediterranean Regional Centroid-moment Tensors Catalog (RCMT). (ed Istituto Nazionale di Geofisica e Vulcanologia) (2002).
58. Pondrelli, S. & Salimbeni, S. Italian CMT Dataset. (ed Istituto Nazionale di Geofisica e Vulcanologia) (2006).
59. Spassiani, I., Taroni, M., Murru, M. & Falcone, G. Real time Gutenberg–Richter b-value estimation for an ongoing seismic sequence: an application to the 2022 marche offshore earthquake sequence (ML 5.7 central Italy). *Geophys. J. Int.* **234**, 1326–1331 (2023).

60. Zhuang, J. C., Ogata, Y. & Wang, T. Data completeness of the Kumamoto earthquake sequence in the JMA catalog and its influence on the estimation of the ETAS parameters. *Earth Planets Space* **69**, 36 (2017).
61. Taroni, M., Selva, J. & Zhuang, J. C. Estimation of the tapered Gutenberg-Richter distribution parameters for catalogs with variable completeness: an application to the atlantic ridge seismicity. *Appl. Sci.* **11**, 12166 (2021).
62. Margheriti, L. et al. Seismic surveillance and earthquake monitoring in Italy. *Seismol. Res. Lett.* **92**, 1659–1671 (2021).
63. Plourde, A. Assessing earthquake rates and b-value given spatiotemporal variation in catalog completeness: application to Atlantic Canada. *Seismica* **2**, <https://doi.org/10.26443/seismica.v2i2.384> (2023).

### Acknowledgements

The authors want to thank the Editor, two anonymous reviewers, and Prof. Peter Bird for their constructive comments that greatly improve the quality of this paper. This work was partially funded by the Centro di Pericolosità Sismica (CPS) at Istituto Nazionale di Geofisica e Vulcanologia (INGV).

### Author contributions

M.T. performed the statistical analyses, MMCC built the deformation model, and both authors outlined the project and wrote the manuscript.

### Competing interests

The authors declare no competing interests.

### Additional information

**Supplementary information** The online version contains supplementary material available at <https://doi.org/10.1038/s43247-023-01059-y>.

**Correspondence** and requests for materials should be addressed to Matteo Taroni.

**Peer review information** *Communications Earth & Environment* thanks the anonymous reviewers for their contribution to the peer review of this work. Primary Handling Editor: Joe Aslin. A peer review file is available.

**Reprints and permission information** is available at <http://www.nature.com/reprints>

**Publisher's note** Springer Nature remains neutral with regard to jurisdictional claims in published maps and institutional affiliations.



**Open Access** This article is licensed under a Creative Commons Attribution 4.0 International License, which permits use, sharing, adaptation, distribution and reproduction in any medium or format, as long as you give appropriate credit to the original author(s) and the source, provide a link to the Creative Commons licence, and indicate if changes were made. The images or other third party material in this article are included in the article's Creative Commons licence, unless indicated otherwise in a credit line to the material. If material is not included in the article's Creative Commons licence and your intended use is not permitted by statutory regulation or exceeds the permitted use, you will need to obtain permission directly from the copyright holder. To view a copy of this licence, visit <http://creativecommons.org/licenses/by/4.0/>.

© The Author(s) 2023